The Planetary Science Journal, 6:177 (7pp), 2025 July https://doi.org/10.3847/PSJ/ade707


# Lucy Mission Search Plans for Activity around Its Jovian Trojan Flyby Targets

S. Alan Stern[1], Carly Howett[2,3], Neil Dello Russo[4], Harold A. Weaver[4], James F. Bell, III[5], Dennis Reuter[6], Amy Simon[6], Hannah Kaplan[6], Keith Noll[6], John Spencer[1], Simone Marchi[1], and Hal Levison[1]
[1] Southwest Research Institute, TX, USA
[2] Planetary Science Institute, AZ, USA
[3] University of Oxford, UK
[4] Johns Hopkins University Applied Physics Laboratory, MD, USA
[5] Arizona State University, AZ, USA
[6] NASA Goddard Space Flight Center, MD, USA
*Received 2025 April 14; revised 2025 June 10; accepted 2025 June 21; published 2025 July 24*

## Abstract

Activity in small bodies, defined here as the episodic or continuous release of material, was long thought to be exclusively a behavior of comets, but it has since been discovered in some centaurs, main-belt asteroids, and near-Earth asteroids. To date, however, no activity has been discovered on Jovian trojan asteroids, the target of NASA's Lucy Discovery Program mission. Although Lucy was originally conceived without studies of or searches for trojan activity, it was realized in 2016–2017 that the spacecraft and scientific payload aboard Lucy could provide unique and meaningful constraints or detections on activity in these trojans. Here we describe how the Lucy mission will search for such activity using (i) its terminal tracking navigation camera to search for wide-field coma scattered light, (ii) its Lucy Long Range Reconnaissance Imager narrow-angle camera to also search for scattered light from any coma or jets, and (iii) its Multispectral Visible Imaging Camera imager to search for CN emission (a common activity tracer species in comets). Sensitivity estimates for each of those measurements are discussed below.

*Unified Astronomy Thesaurus concepts:* Jupiter trojans (874); Small Solar System bodies (1469); Coma dust (2159); Neutral coma gases (2158)

## 1. Activity in Distant Small Bodies

During their formation in the outer solar system, Jovian trojans almost certainly accreted volatile ices. However, it is an open question how much ice has been retained during their long storage near 5.2 au from the Sun, and whether these objects presently display weak, long-term, or perhaps stronger, sporadic, and active, outgassing and/or shedding of surface material.

Regarding this, it is notable that a modest fraction (i.e., ∼10%) of the known centaurs, orbiting farther from the Sun than the Jovian trojans, do display comae and are active (e.g., J. M. Bauer et al. 2013), though such activity often (but not always) correlates with objects that have undergone recent orbit changes bringing them closer to the Sun. The activity observed in centaurs, plus the periodic activity seen in some main-belt asteroids (e.g., D. Jewitt et al. 2015), suggests that some Jovian trojans could also show comet-like activity, at least at some times. In fact, activity has been detected in comet P/2019 $LD_2$ (ATLAS), which was originally thought to be a Jupiter trojan, though we note that subsequent orbit determinations reclassified this object as a centaur (B. T. Bolin et al. 2021; H. H. Hsieh et al. 2021; T. Kareta et al. 2021; J. Licandro et al. 2021). Additionally, although remote sensing observations have so far failed to detect coma dust or outgassing associated with any Jupiter trojan (e.g., S. Bagnulo et al. 2016), near-IR reflectance spectroscopy of the Lucy trojan flyby targets with JWST shows evidence for $H_2O$ (through its tracer, OH), as well as trapped $CO_2$ and surface organics (I. Wong et al. 2024). It is therefore of natural interest to search for both volatile species and coma gas and dust around the Lucy trojan flyby targets.

## 2. Lucy Activity Search Rationale and Background

The rationale for the Lucy mission to search for activity in the mission's trojan flyby targets is guided by the desire to make the mission as valuable as is feasible, and to maximize the leap in knowledge that Lucy delivers regarding the Jovian trojans (e.g., H. F. Levison et al. 2021; K. S. Noll et al. 2023). To this end, in 2017 the Lucy mission science leadership formed a Trojan Activity Working Group (TAWG; S. Marchi et al. 2023).

TAWG began its work by conducting a broadly based review of the capabilities of Lucy's scientific instruments (C. B. Olkin et al. 2021; K. S. Noll et al. 2023) to detect dust/particulates and/or gas around its trojan flyby targets. Each resulting detection concept was then studied to determine its ability to deliver better results than could be obtained by non-Lucy (i.e., Earth-based and other space-based) facilities. This sieving of concepts is important because it protects valuable spacecraft (e.g., propellant, pointing time, bandwidth, data storage) and team resources (e.g., labor) from being spent on efforts for Lucy to detect trojan activity that could be better accomplished by other means.

After quantifying the expected Lucy trojan activity detection capability from each proposed concept, comparing those to existing ground-based and space-based capabilities, and applying the criterion that the mission will only execute activity searches where Lucy yields better results, coma dust and coma gas trojan activity measurement techniques

involving three Lucy instruments were found to be of sufficient value to implement in flyby planning for its trojan flyby targets. These techniques are:

1. Dust searches using panchromatic imaging by both the Lucy Long Range Reconnaissance Imager (L'LORRI; H. A. Weaver et al. 2023) and Terminal Tracking Camera (TTCam; J. F. Bell et al. 2023) instruments, from regions surrounding the trojan flyby targets.
2. CN fluorescence emission searches using the L'Ralph instrument's (D. C. Reuter et al. 2023) filter imaging to search for 3883 Å resonance fluorescence from CN molecules in the vicinity of the mission's trojan targets. (We note that 3883 Å CN emission has long been used as a tracer of distant cometary activity (e.g., M. F. A'Hearn 1982), owing to the exceptionally high 3883 Å CN (0–0) resonance fluorescence $g$-factor of the CN molecule.)

A summary table with some relevant instrument parameters for these searches is given below in Table 1.

In the next three sections of this paper, we review how each instrument will undertake these activity search observations, their expected detection sensitivities, and observing strategies.

## 3. L'LORRI Activity Search Measurement Techniques and Expected Detection Limits

Ground-based remote sensing techniques can detect dust in the coma of trojans to a limit of about $Af\rho \sim 10$ cm (e.g., S. Bagnulo et al. 2016); $Af\rho$ is a standard measurement metric for the dustiness of cometary comae (e.g., M. F. A'Hearn 1982). However, based on instrument sensitivity and the geometry of encounter scenarios, dust lifted off the surfaces of trojans can be detected by the L'LORRI instrument to a limit of about $Af\rho \sim 1$ cm. This is equivalent to dust production rates of $\sim$0.01–0.1 kg s$^{-1}$, depending on the particle size distribution. This is similar to, or less than, the activity levels measured in main-belt comets (e.g., H. H. Hsieh & S. S. Sheppard 2015; F. J. Pozuelos et al. 2015; J. Agarwal et al. 2017; J. A. Fernandez et al. 2017). Furthermore, few additional spacecraft resources are needed for Lucy to obtain these more stringent constraints, or perhaps detections, on trojan activity, as much of the imaging needed for coma searches/detections can be done using optical navigation (OpNav) images and high-resolution trojan science images already planned near closest approach.

The general strategy for searching for particulates around Lucy's trojan targets using the L'LORRI instrument involves obtaining observations at favorable solar elongation angles (i.e., Sun–L'LORRI trojan solar elongation angles (SEAs)) and solar phase angles (i.e., Sun–trojan–L'LORRI angles (SPAs)) during each trojan flyby. The trojan dust phase function is unknown, so we assume for predictive modeling purposes two possible trojan dust analogs: (1) a composite comet dust phase function from ground-based comet observations (D. Schleicher 2010), and (2) the Rosetta Optical, Spectroscopic, and Infrared Remote Imaging System (OSIRIS) dust phase function for comet 67P Churyumov-Gerasimenko (F. Moreno et al. 2018).

Extensive calibration work has been done to characterize L'LORRI sensitivities as a function of SEA, which have been found to drop rapidly for SEAs $< 90^\circ$ owing to stray light. Lucy plans to use two types of L'LORRI measurements to search for dust around trojans during encounters.

The first of these is to make deep imaging integrations when its flyby Jovian trojans are unresolved. Based on experience from the Lucy encounter with the Dinkinesh/Selam system (H. F. Levison et al. 2024), these measurements can mostly, if not completely, be satisfied using L'LORRI OpNav approach images. Because the properties of the point-spread function (PSF; FWHM 2.7 L'LORRI pixels) are well understood, and many stars are also imaged with these OpNav images (H. A. Weaver et al. 2023), any extended sources around the flyby targets can be sensitively differentiated from a no-coma trojan point-source PSF. To optimize sensitivity, such images can be spatially coregistered and coadded. Signal in excess of a no-coma PSF detected over concentric annuli of increasing distance can then be determined and converted to an $Af\rho$ detection limit or detection value (see Figure 1).

The second kind of L'LORRI trojan activity search measurement obtains imaging when flyby targets are resolved (i.e., the trojan's diameter exceeds the L'LORRI resolution limit of $\sim$2.7 pixels), taking the deepest practical exposures on their dark limbs (typically with exposure times smaller than $\sim$10 s to reduce image motion smear). Much of this imaging can be obtained with rotational coverage images, but additional imaging is also planned. Individual images can be examined frame by frame with the appropriate intensity stretch display, after removing cosmic rays and CCD artifacts. The spatial morphology of detected dust coma can be used to differentiate isotropic outflow from discrete jets. When possible, any coma morphology will be mapped to specific surface regions.

Such L'LORRI images will also be sensitive to meter-sized boulders near the trojans. For any detections of such objects, brightness can be measured and converted to an apparent visual magnitude ($V$mag) to estimate an effective diameter. Detectability limits can then be determined if no boulders are detected by emplacing "fake boulders" of varying brightness in images (see Figure 2). This technique suggests an upper limit to boulder sizes within the field of view (FOV) for Dinkinesh of approximately 1 m (again, see Figure 2). Detection limits on boulder trojan sizes are also expected to be $\sim$1 m (K. S. Noll et al. 2023) but will depend on integration times, the distance of imaging from the target, and the SEAs of the observations. More specifically, based on TTCam's radiometric sensitivity (Y. Zhao et al. 2024), boulders $\geqslant$1 m in size should be detectable at SNR $\geqslant 2$ in single $\sim$2 s exposure images, and objects down to $\sim$300 cm should be detectable in the longest possible single 30 s exposure images, assuming an albedo of 0.04 for any such objects and observations at typical approach and departure ranges from the trojan targets.

These $V$mags correspond to effective spherical diameters of 1.07, 1.39, and 1.96 m for the $3\sigma$, $5\sigma$, and $10\sigma$ cases, respectively. This suggests an upper limit to boulder sizes within the FOV for Dinkinesh of approximately 1 m. Similar detection limits on boulder sizes are expected at the trojans. How close to the target such detections can be made depends on the size (and hence the brightness) of the boulders, but a rough estimate is that a 2 m boulder could be detected if it is $>$2.5 km projected distance ($\sim$30 pixels) from its trojan primary, assuming such a boulder does not land on an image artifact.

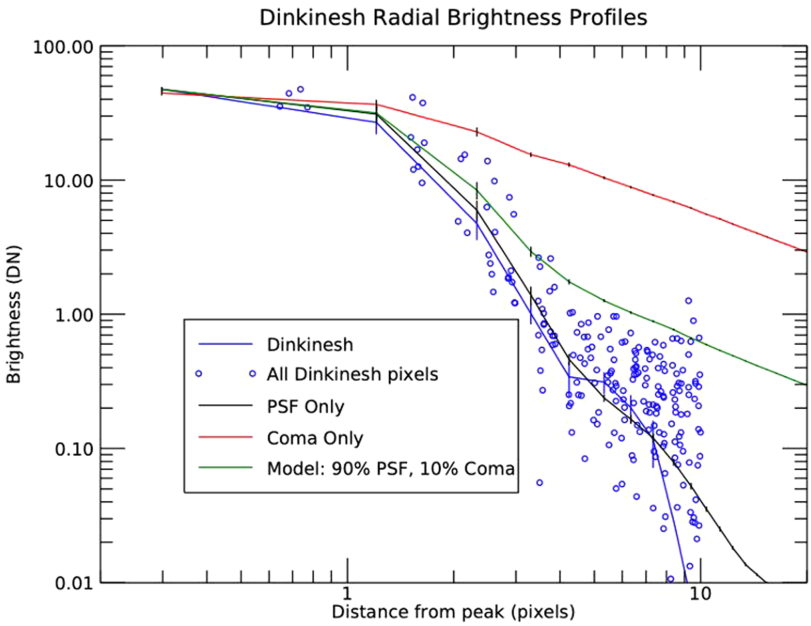


**Figure 1.** Dinkinesh radial brightness profile showing counts in pixels with increasing radial distance from the center of brightness (blue circles) obtained on UT 2023 October 26 using a coadd of eight 20 s images. For these data, the range to target was $2.4 \times 10^6$ km and the Sun–probe angle (SPA) was 117.°5. Both a PSF brightness profile with no coma (black curve) and a coma brightness profile (red curve), assuming a spherical symmetric coma with a $1/r$ brightness profile (where $r$ is the projected distance from the peak) are shown. The observed Dinkinesh profile is consistent with no or little coma. A model brightness represented by 90% PSF and 10% coma sets a reasonable upper limit to a dust coma, yielding an upper limit for $Af\rho < 0.94$ cm at SPA = 117.°5, and $Af\rho < 0.72$ cm corrected to SPA = 0° using the D. Schleicher (2010) phase law for ensemble cometary dust.

**Table 1**
Selected Lucy Instrument Summary Parameters

| Parameter | L'Ralph MVIC | L'LORRI | TTCAM |
|---|---|---|---|
| Field of view (deg) | 8.29 × 8.02 | 0.289 × 0.298 | 11.0 × 8.2 |
| Resolution pixel$^{-1}$ (iFOV; $\mu$rad) | 28.8 | 4.9355 | 74.1 |
| Active pixels ($x$ versus $y$; band$^{-1}$) | 5024 × 64 | 1024 × 1024 | 2592 × 1944 |
| PSF FWHM (pixels) | Pan: 1.70 ± 0.21; Violet: 1.66 ± 0.30; Green: 1.62 ± 0.29; Orange: 1.60 ± 0.31; Phyllo: 1.64 ± 0.38; NIR: 1.64 ± 0.38 | 2.7 | 1.3 |

## 4. L'Ralph Activity Search Measurement Techniques and Expected Detection Limits

One way to determine if primitive ices are still present on the Jupiter trojans is to determine if there are measurable levels of outgassing observable as coma activity. Such activity is not unprecedented. For example, S. J. Bus et al. (1991) detected CN emission from Chiron at 11 au, which was predicted to be from outbursts of CO or other supervolatiles, and which was later confirmed (M. Womack & S. A. Stern 1999). Emission was observed extending over 50,000 km (∼10″ as seen from Earth). Later, photometric evidence even emerged of Chiron having been active at its 18.9 au aphelion (S. J. Bus et al. 2001).

The Lucy L'Ralph Multispectral Visible Imaging Camera (MVIC) has five color channels (violet 375–480 nm; green 480–520 nm; orange 520–625 nm; phyllosilicate 625–750 nm; and near-infrared 750–900 nm) and one panchromatic channel (350–950 nm; D. C. Reuter et al. 2023). CN emission occurs in this wavelength range due to a range of vibrational bands: $\Delta v = +\mathbf{1}$(358–360 nm), $\Delta v = \mathbf{0}$(358–389 nm, strongest), and $\Delta v = -\mathbf{1}$(415–422 nm), with the strongest absorption due to the (0–0) vibrational band at 388.29 nm (e.g., S. J. Mousavi et al. 2015). As noted above, this band has long been used to detect distant activity in comets owing to its extraordinarily high resonance fluorescence efficiency in sunlight, i.e., its high $g$-factor. Both MVIC's violet and panchromatic channels cover these CN emission wavelengths.

### 4.1. MVIC's Sensitivity to CN

To determine whether MVIC could detect a Chiron-like level of CN emission, we determined the predicted signal-to-noise ratio (SNR) for such emission at 5 au (the location of the trojan asteroids). For feasibility calculations, we adopt a minimum SNR = 5 (the Rose criterion; see A. E. Burgess 1999) for detection; of course, SNR ≫ 5 would be preferable.

As above, Chiron was at 11 au when CN was detected at the rate of $5.7 \times 10^{-15}$ erg cm$^{-2}$ s$^{-1}$ (S. J. Bus et al. 1991), when adjusted for higher sublimation rates and a brighter Sun at 5 au scales to $6 \times 10^{-9}$ erg cm$^{-2}$ s$^{-1}$. To then calculate MVIC's SNR for this flux, the spectral response (SR) has to first be determined. We assume a spectrally dependent quantum efficiency of 0.05 at 388 nm, a filter transmittance of 1.0, a mirror reflectance of 0.95 for each of MVIC's five mirrors, and a dichroic filter transmittance of 0.90. The SR is calculated as a product of these quantities, and is thus estimated to be

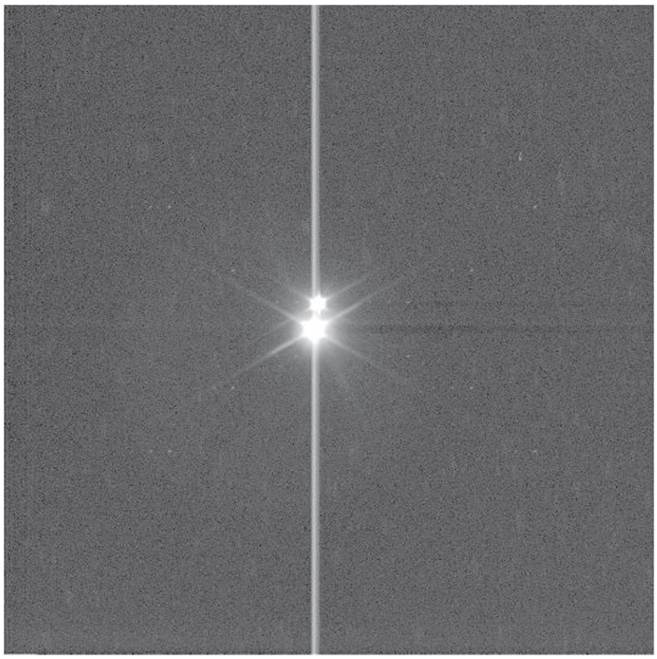

**Figure 2.** Testing the size detectability limits for boulders near Dinkinesh. A composite of 8300 ms Dinkinesh flyby images (the frame covers $0.^{\circ}29 \times 0.^{\circ}29$; Dinkinesh and Selam are the two brightest objects in the field) obtained on UT 2023 November 1, displayed using an inverse hyperbolic sine function stretch from 0 to 100 DN. Synthetic objects are marked with red circles. Here, one L'LORRI pixel subtends 79 m projected distance at Dinkinesh (range to target ~16,000 km) and has an SPA = $59.^{\circ}24$. Fake objects were inserted at 36 different locations with peak signals $3\sigma$, $5\sigma$, and $10\sigma$ above the nominal noise level ($1\sigma \approx 0.36$ DN); it was found that even $3\sigma$ objects appear to be detectable over most of the FOV. Fake objects had $V$mag = 15.09, 14.54, 13.79 for the $3\sigma$, $5\sigma$, and $10\sigma$ cases, respectively, assuming for their phase law that $G = 0.378$, geometric albedo $p_v = 0.287$, and an S-type asteroid spectral energy distribution. (S-type asteroids have moderately steep slope at wavelengths shorter than 0.7 $\mu$m; moderate to weak absorption features around 1 $\mu$m and 2 $\mu$m, indicating the presence of silicates; and a broad but shallow absorption feature centered near 0.63 $\mu$m, sometimes present. They have similar spectral characteristics to certain stony meteorites, suggesting a possible connection. S-types are dominant in the near-Earth population and the inner asteroid belt (<2.2 au from the Sun) and are common in the central belt (~3 au) but rare farther out. Examples include (3) Juno, (15) Eunomia, (7) Iris, and (433) Eros.) This image is a composite of 10 L'LORRI images with a FOV of $\sim 0.^{\circ}29$. Dinkinesh is the brightest spot and is about 0.82 × 0.45 × 0.77 km in extent.

$3.48 \times 10^{-2}$. The predicted signal for the full coma can then be calculated by taking the product of the SR, the coma flux ($6 \times 10^{-9}$ erg cm$^{-2}$ s$^{-1}$, or 1173 photons cm$^{-2}$ s$^{-1}$ assuming the CN emission is dominated by the 388.29 nm line), the area of MVIC's aperture (diameter 7.5 cm; D. C. Reuter et al. 2023) and a unity yield from photons to electrons. Using the values given produces an estimated signal of 1803 electrons s$^{-1}$. D. C. Reuter et al. (2023) showed MVIC's dominant noise source is its electronics noise (which includes the read noise) and is estimated to be 20 electrons. Thus, we can assume this signal has a corresponding noise of 46.9 electrons (using total noise = $\sqrt{\text{signal} + (\text{electronics noise})^2}$, and thus an SNR of 38.4 for an integration of 1 s.

However, a coma is not a point source. If we assume a Chiron-like coma that covers 10″ (48.5 $\mu$rad; S. J. Bus et al. 1991), this is equivalent to a 12,000 km diameter coma as seen from 0.1 au. The size of the coma ($5 \times 10^{-7}$ str if converted to solid angle) is ~600× larger than MVIC's 28.8 × 28.8 rad (or $8.3 \times 10^{-10}$ str) instantaneous FOV (iFOV; D. C. Reuter et al. 2023). S. J. Bus et al. (1991) were able to fit the observation with a uniform brightness over the 10″ diameter (at which point it linearly decreases out another 5″ on either side). Thus, we assume here that the coma signal is equally split over ~600 MVIC pixels. This results in the predicted CN total signal of 1803 electrons s$^{-1}$being split into ~3 electron s$^{-1}$ for a single MVIC pixel.

MVIC's integration time depends upon the observation scan time and instrument settings. MVIC works via time delay integration (TDI), so the charge can be transferred in either 4, 8, 16, 32, or 64 along-track rows (D. C. Reuter et al. 2023), thus enabling a range of integration times for a given scan rate. For our 12,000 km coma at 0.1 au distance (i.e., every MVIC pixel covers 435 km at the target), 27 along-track pixels will need to be covered. If an MVIC clocking time of 0.5 s row$^{-1}$ is assumed (set to be comfortably faster than the 0.66 s row$^{-1}$ minimum), then a total integration time of 14 s is required to scan the coma. This results in a final signal per pixel of 42 electrons, leading to a noise (using the same assumptions as above) of 21 electrons, and thus a SNR of 2. However, we note in that practice, the number of along-track pixels will be set to an integer of the number of TDI rows (so at least 32).

This SNR can be increased by performing analog pixel summing on board the instrument in the along-track and/or cross-track direction. The number of pixels in each track to sum across can be set independently. This has the advantage of increasing the signal without notably increasing the noise. Examples of various analog pixel summing regimes are shown in Table 2. As the table shows, analog binning alone is unlikely to produce very high (>100) SNR, but it does produce a significant increase to SNR > 5 by 2 × 2 binning alone.

Additional analysis of downlinked images on Earth can be used to further increase the SNR. However, coadding pixels in returned images increases the noise as well as the signal, so the SNR increases by a factor of $\sqrt{N}$, where $N$ is the total number of coadded pixels. This applies to pixels coadded in the same image (decreasing the spatial resolution), or the pixel covering the same region in different images (maintaining the spatial resolution but requiring more images).

### 4.2. Developing an MVIC Observing Strategy

Three different strategies for detecting coma activity by MVIC have been considered. The first is increasing the number of MVIC observations tailored for coma detection. This technique retains the highest spatial resolution but requires many images to provide a significant SNR increase. For example, for a single pixel to increase the SNR from 2 (Table 2) to 25 (or 100) for a Chiron-like coma CN detection, 25 (or 2500) images would need to be returned, respectively. Obtaining large numbers of images comes at a high labor cost (sequencing the observations and returning the data) and a high data volume cost.

The second strategy is to allow onboard analog pixel summing. Since the coma is likely to be an extended object, losing some spatial resolution to gain significant SNR is a potentially worthwhile trade. However, due to its nature, this decision has to be built into the observation design and is thus irreversible.

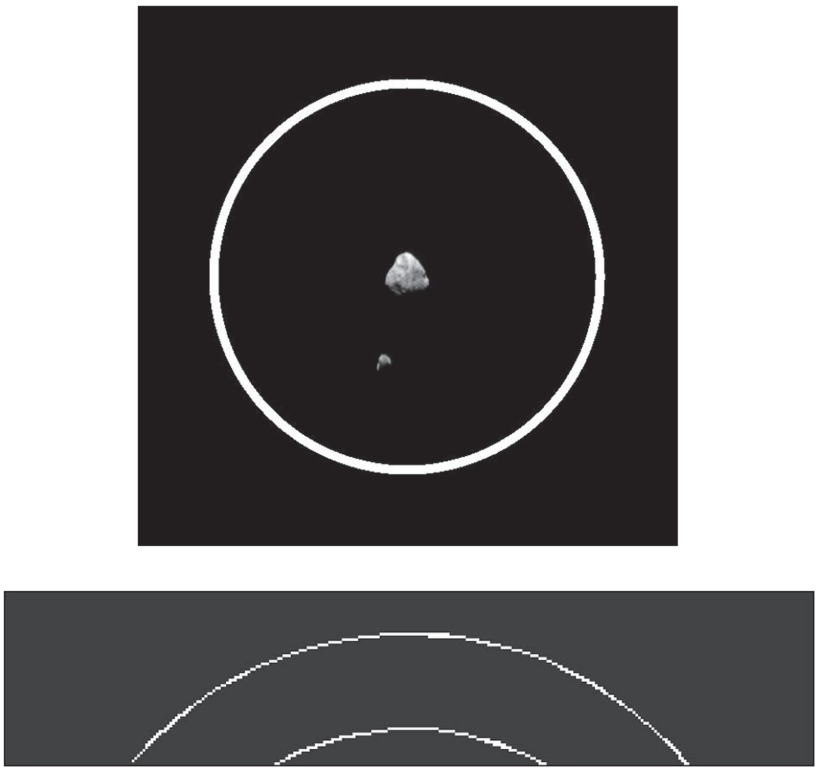

**Figure 3.** Subsection of the MVIC FOV showing possible annuli addition configurations. Top: coadding profile for a target centered in the FOV (used for distant observations). A 601 × 601 pixel example is given, which could be the full in-track spatial extent but would only be a small part (601 of 5000 pixels) of the cross-track extent. The white circle shows the extent of the 10 pixel annulus that is summed over. The observation used is a violet MVIC observation of Dinkinesh taken on 2023 November 1 at 16:53:27.778 UTC. Bottom: coadding profile of a target centered outside the FOV (used for close observations). Only a subset of the MVIC FOV is shown (64 × 300 pixels). In this example, the extent of the annuli is from the inner to the outer circle, which have diameters of 270 and 200 pixels (shown at a width of 1 pixel). The target (not shown) is assumed to be at the center of the annuli, outside the FOV. There is no scale shown, because different images have differing scales during approach to and then departure from each flyby target.

**Table 2**
L'Ralph SNR for Various Pixel Summing Sizes

| Pixel Summing (Along Track × Cross Track) | 1 × 1 | 1 × 2 | 2 × 2 | 3 × 2 | 3 × 4 | 4 × 4 |
|---|---|---|---|---|---|---|
| Signal (electrons) | 42 | 85 | 169 | 254 | 507 | 676 |
| SNR | 2 | 4 | 7 | 10 | 16 | 20 |

**Notes.** This table assumes a detector noise of 21 electrons (see text). The pixels can be in either the along-track or cross-track directions; note that any value can be summed in the TDI directions, but there are limitations on the allowed cross-track summing modes (only 1, 2, 4, or 8 are allowed).

The final strategy is to build the capability to coadd pixels on the ground to increase the SNR, specifically those located in concentric annuli centered on the target on the returned images (see Figure 3). By assuming the activity is isotropic, this binning allows the CN emission as a function of distance from the target to be determined. The width of the annuli can be altered to trade between spatial resolution and SNR. The SNR increase would depend upon the width of the chosen annuli, but to indicate the maximum capability of this strategy, the CN emission from the entire coma could be compared against the background. If we assume 600 MVIC pixels are filled by a uniformly emitting coma against a zero-noise sky then, coadding across these single pixels, the coma provides a CN detection SNR of 49. The tool to produce such binning for MVIC data is in development and is being tested on the data from asteroid 152830 Dinkinesh for use in the 52246 DonaldJohanson asteroid encounter in 2025 April.

### *4.3. Implemented Strategy*

Lucy's first encounter with a Jupiter trojan is with Eurybates on 2027 August 12. The observation sequence is currently in development, and the techniques discussed have been adopted to enable MVIC to search for CN emission as a tracer for activity. Through discussion within the Lucy team, the number of MVIC coma observations was increased from one to four for each trojan encounter. This doubled the SNR without adding a significant resource burden onto the mission. Two observations will be taken on the inbound and two on the outbound, each at 0.01 au from the target. The observations scan ±12,000 km across the target, and will be made at 58 $\mu$rad s$^{-1}$ using 64 TDI rows for all channels. Thus, although the CN emission will predominantly be detectable by the violet channel, all colors (including panchromatic) will be obtained. This enables any changes detected in the violet to be verified with panchromatic observations and activity to be searched for

across the entire MVIC wavelength coverage, and not just in MVIC's CN emission channels.

As a compromise between SNR and spatial resolution, the initially planned coma observations for Eurybates are to utilize analog pixel summing, thus proving an increase in signal (see Table 2). Additional pixel binning across the images will be done using the tools described as required. The binning for other encounters can be adjusted based on this result.

## 5. TTCam Activity Search Measurement Techniques and Expected Detection Limits

The Lucy TTCam (C. B. Olkin et al. 2021; J. F. Bell et al. 2023) will also be used to search for evidence of activity around the mission's Jovian trojan asteroid flyby target bodies. TTCam is a wide FOV ($11^\circ \times 8.^\circ 2$) broadband (425–675 nm) digital imager system based on a $2752 \times 2004$ pixel monochrome complementary metal oxide semiconductor sensor. The simple measurement approach employed for TTCam activity is similar to that used by L'LORRI and L'Ralph MVIC as described above, but it exploits the much larger TTCam FOV, compared to the other Lucy imaging instruments, to search more of the volume around and along the limb of each flyby target.

TTCam observation modes are constrained in terms of timing by the priority for the camera to be performing its primary function, i.e., to provide an autonomous onboard late pre-encounter update of the location of each trojan asteroid flyby target relative to the spacecraft (P. G. Good et al. 2022). Necessarily, observations designed to detect activity within the time devoted to terminal tracking (typically within the final minutes of each close approach) will be very short exposure time images (ranging from ~1 ms to a few tens of milliseconds) acquired at a regular cadence ~13–15 s apart.

Beyond their use for the tracking function, TTCam images will also be useful for helping to assess the geology and shape of each asteroid target, because at the planned flyby distances, none of the trojan targets are expected to overfill the TTCam FOV. Thus, the TTCam image data set for each flyby will provide "whole disk" views of the entirety of the sunlit surface of each target body, at pixel scales around 30–90 m pixel$^{-1}$, depending on the specific flyby distances. Of specific relevance to the search for activity, the entire limb and terminator will be continuously visible in TTCam images of the object during each flyby, allowing a sensitive search for any jetting or other mass loss evidence, such as faint coma, against the dark space background.

Conversely, outside of the time devoted to terminal tracking, two sets of much longer (up to 30 s) exposure time images will be acquired: one set shortly before and one shortly after closest approach. Each set will consist of up to 12 long-exposure images, used to filter out cosmic rays, increase SNR via image summing, and enable a limited amount of tracking of any detected objects or activity. These images will be acquired typically from ~10,000 to ~50,000 km distances from each flyby target, and thus will cover a plane-of-sky area extending from ~1000 to ~5000 km in radius from each target. This represents a significant fraction of the Hill radius of stability for each flyby trojan, and an even larger fraction of each trojan flyby target's more stable Szebehely radius of stability.

TTCam's radiometric sensitivity was assessed via preflight calibration measurements and refined and validated based on observations of the Moon during the Lucy mission's 2022 October Earth gravity assist flyby (Y. Zhao et al. 2024). Assuming that shed objects have an $I/F$ (intensity divided by solar flux) of 0.04 and are observed at 5 au from the Sun and from a closest-approach flyby distance of 1000 km, TTCam's sensitivity indicates that SNRs of ~2 to ~50 could be achieved for objects from 10 to 100 m in diameter, respectively, in only ~35 ms exposure times, consistent with the expected exposure times during tracking mode observations of each flyby target. Smaller objects would require exposure times longer than currently planned for nominal terminal tracking function observations.

For longer-exposure TTCam observations outside of the encounter times devoted to terminal tracking, exposure times of ~2.5 s and ~25 ms would be required to achieve SNRs $\geqslant 2$ for the same 10–100 m diameter objects, respectively, if observed from a range of 10,000 km from the target. Those exposure times increase to 600 ms and 60 s at 50,000 km target distance. Since the maximum TTCam exposure time is only 30.7 s, the desire to be sensitive to ~10 m size objects at the largest potential target distances expected for "closest possible" long-exposure TTCam imaging drives the need to coadd multiple 30 s observations to increase SNR.

The search for potential faint coma-like signals around each of the trojan flyby targets also drives the need for coadding multiple 30 s TTCam exposures. For example, if an $I/F$ of the coma that was observed at comet 67P Churyumov-Gerasimenko is assumed ($\sim 2 \times 10^{-7}$ at 2.39 au; I. Bertini et al. 2017) and scaled to 5 au, then for the maximum 30 s exposure time, TTCam SNR per pixel for extended-source (multipixel filling) coma is predicted to be only ~1.1 for a coma that is all reflected sunlight. Coma $I/F \geqslant \sim 3.7 \times 10^{-7}$ at 5 au would be needed to achieve SNR per pixel $\geqslant 2$ in a single 30 s TTCam image. Thus, the detectability of faint extended comas near or around the Lucy trojan targets will depend strongly on the actual $I/F$ of the coma itself, supporting a relatively simple strategy of coadding as many individual 30 s images as resources allow to maximize the ability to detect as low $I/F$ coma as possible.

TTCam tracking mode and activity search images will be calibrated to $I/F$ (Y. Zhao et al. 2024) and analyzed using standard coadding, image stacking, and image blinking methods to filter out cosmic rays and to search for evidence of nonstellar and potentially moving objects in the vicinity of each flyby target. Evidence for faint coma signal in both close-approach tracking mode images and more distant long-exposure images will utilize a similar annular summing method as described above for the MVIC coma search images.

## 6. Summary

In this report, we have summarized the rationale for activity searches during the flybys of the Lucy mission Jovian trojan targets. We have also briefly described how both searches for and detections of such activity, if present, bear on trojan asteroid science. We then described the three separate measurement techniques that the Lucy mission will use to search for trojan activity and provided the quantitative detection limits expected from each. To summarize these measurement techniques briefly, two use the L'LORRI and TTCam panchromatic imager to search for particulate scattering in the putative atmosphere/coma of the flyby Jovian trojan targets, and one uses the L'Ralph MVIC color imager to search for evidence of gas emission from the 3883 A emission line of CN gas, a well-known molecular tracer of distant activity in comets.

In each case, we quantified the search sensitivity limits that these techniques can achieve and described the observational strategies for each search. This paper therefore serves as a summary of the archival literature of the Lucy trojan activity search objectives, methods, techniques, and expected sensitivities.

## Acknowledgments

The authors acknowledge and thank NASA for support of the Lucy mission, which is funded through the NASA Discovery program on contract No. NNM16AA08C. The authors also thank the two anonymous referees.

## ORCID iDs

S. Alan Stern https://orcid.org/0000-0001-5018-7537
Carly Howett https://orcid.org/0000-0003-1869-4947
Neil Dello Russo https://orcid.org/0000-0002-8379-7304
Harold A. Weaver https://orcid.org/0000-0003-0951-7762
Amy Simon https://orcid.org/0000-0003-4641-6186
Hannah Kaplan https://orcid.org/0000-0002-6562-9462
Keith Noll https://orcid.org/0000-0002-6013-9384
John Spencer https://orcid.org/0000-0003-4452-8109
Simone Marchi https://orcid.org/0000-0003-2548-3291
Hal Levison https://orcid.org/0000-0001-5847-8099

## References

Agarwal, J., Jewitt, D., Mutchler, M., Weaver, H., & Larson, S. 2017, Natur, 549, 357
A'Hearn, M. F. 1982, in Comets, ed. L. Wilkenning (Tucson, AZ: Univ. Arizona Press), 433
Bagnulo, S., Belskaya, I., Stinson, A., Christou, A., & Borisov, G. B. 2016, A&A, 585, A122
Bauer, J. M., Grav, T., Blauvelt, E., et al. 2013, ApJ, 773, 22
Bell, J. F., III, Zhao, Y., et al. 2023, SSRv, 219, 86
Bertini, I., La Forgia, F., Tubiana, C., et al. 2017, MNRAS, 469, S404
Bolin, B. T., Fernandez, Y. R., Lisse, C., , M., et al. 2021, AJ, 161, 116
Burgess, A. E. 1999, JOSAA, 16, 633
Bus, S. J., A'Hearn, M. F., Bowell, E., & Stern, S. A. 2001, Icar, 150, 94
Bus, S. J., A'Hearn, M. F., Schleicher, D. G., & Bowell, E. 1991, Sci, 251, 774
Fernandez, J. A., Licandro, J., Moreno, F., et al. 2017, Icar, 295, 34
Good, P. G., Faiks, P., & Pisano, W. J. 2022, in 44th Annual AAS Guidance, Navigation and Control Conf., ed. M. Sandnas & D. B. Spencer (Berlin: Springer), 1253
Hsieh, H. H., Fitzsimmons, A., Novakovic, B., Denneau, L., & Heinze, A. N. 2021, Icar, 354, 114019
Hsieh, H. H., & Sheppard, S. S. 2015, MNRAS, 454, L81
Jewitt, D., Hsieh, H., & Agarwal, J. 2015, in Asteroids IV, ed. P. Michel et al. (Tucson, AZ: Univ. Arizona Press), 221
Kareta, T., Woodney, L., , M., Schambeau, C., et al. 2021, PSJ, 2, 48
Levison, H. F., Marchi, S., Noll, K. S., et al. 2024, Natur, 629, 1015
Levison, H. F., Olkin, C. B., Noll, K. S., et al. 2021, PSJ, 2, 171
Licandro, J., De Leon, J., Moreno, F., et al. 2021, A&A, 650, A79
Marchi, S., Bell, J. F., III, Bierhaus, B., & Spencer, J. 2023, SSRv, 219, 44
Moreno, F., Guirado, D., Munoz, O., et al. 2018, AJ, 156, 237
Mousavi, S. J., , H., Farsani, M., Darbani, S. M. R., et al. 2015, ApOpt, 54, 1713
Noll, K. S., Brown, M. E., & Buie, M. W. 2023, SSRv, 219, 59
Olkin, C. B., Levison, H., Vincent, M., et al. 2021, PSJ, 2, 172
Pozuelos, F. J., Cabrera-Lavers, A., Licandro, J., & Moreno, F. 2015, ApJ, 806, 102
Reuter, D. C., Simon, A. A., Lunsford, A., et al. 2023, SSRv, 219, 69
Schleicher, D. 2010, Lowell Minor Planet Services, https://asteroid.lowell.edu/comet/dustphase_details.html
Weaver, H. A., Wilson, J. P., Conard, S. J., et al. 2023, SSRv, 219, 82
Womack, M., & Stern, S. A. 1999, SoSyR, 33, 187
Wong, I., Brown, M. E., Emery, J. P., et al. 2024, PSJ, 5, 87
Zhao, Y., Bell, J. F., III, Sahr, E., et al. 2024, E&SS, 11, e2024EA003576